Maximizing the optical performance of planar $CH_3NH_3PbI_3$ hybrid perovskite heterojunction stacks

Laurie J. Phillips[a,*], Atef M. Rashed[a], Robert E. Treharne[a], James Kay[a], Peter Yates[a], Ivona Z. Mitrovic[b], Ayendra Weerakkody[b], Steve Hall[b], Ken Durose[a]

[a]*Stephenson Institute for Renewable Energy, University of Liverpool, Liverpool, L69 7ZF, UK*
[b]*Department of Electrical Engineering and Electronics, University of Liverpool, Brownlow Hill, Liverpool, L69 3GJ, UK*

Abstract

A vapour-phase reaction process has been used to deposit smooth and uniform $CH_3NH_3PbI_3$ perovskite material to enable the measurement of its optical dispersion relations, n & k, by ellipsometry. Fitting was achieved with a combination of Tauc-Lorenz, critical point parabolic band (CPPB) and harmonic oscillators. We have used the dispersion relations in an all-optical model of new planar device architectures in order to establish design rules for future materials choices to maximise the short-circuit current (J_{sc}) performance. For 500 nm of MAPI with no window layer, the maximum performance expected from the model is J_{sc} = 21.63 mA cm^{-2}. The ability of thin layers (in the range 20 - 60 nm) of a range of window layer materials (TiO_2, WO_3, ZnO, Nb_2O_5, CdS, and $Cd_{0.4}Zn_{0.6}S$) to enhance the short-circuit current of the devices was investigated. The performance of the oxides showed interference behaviour, with the first maxima in their J_{sc} curves exceeding the value achievable without a window layer. However, after the first maximum, the performance generally fell off with increasing thickness. The only material to stay greater than the no-window condition for the entire investigated range is WO_3. The highest performance (J_{sc} of 22.47 mA cm^{-2}) was obtained with 59 nm of WO_3, with that of TiO_2, ZnO, and Nb_2O_5 being marginally lower. Parasitic absorption in CdS window layers caused the J_{sc} to decrease for all non-zero thicknesses - it gives no interference enhancement and its use cannot be recommended on optical grounds. Use of the wider gap alloy $Cd_{0.4}Zn_{0.6}S$ gave higher currents than did CdS but its performance was not so high as for the oxides. Observations are made on the practicalities of fabricating the target structures in the fabrication of practical PV devices.

1. Introduction

Hybrid organic-inorganic perovskite absorbers have recently emerged as highly promising materials for next-generation photovoltaics. They have the perovskite lattice, can be prepared from solution at low temperatures (<150 °C) and use abundant elements. Historically, most photovoltaic technologies have increased in efficiency at ~ 0.5% per year. In contrast, the rate of development for perovskite-based cells has been unprecedented, with the best certified efficiency increasing from 3.8% to 20.1% in less than five years.[1–4] This increase, an order of magnitude quicker than competing technologies, will mean that efficiencies could reach 25% by 2015, rapidly approaching the Shockley-Queisser limit.

If this trend is to continue, optimization will be required of not just the absorber, but the complete heterojunction stack. Organic-inorganic perovskites have been shown to possess exceptionally good charge transport properties for photovoltaic applications. Methyl ammonium lead tri-iodide, $CH_3NH_3PbI_3$ (MAPI) has long carrier lifetimes, particularly when prepared from a mixed halide precursor material, and has exhibited electron-hole diffusion lengths in excess of 1 µm.[5–9] Additionally, the exciton binding energy for MAPI has been measured to be ~ 50 meV, indicating that the photovoltaic operation of the cell is due to free-carriers rather than exciton ionisation, as in the case of a dye-sensitized solar cell.[10] These properties suggest that high-efficiency devices do not rely on a mesoporous scaffold layer for exciton splitting and charge extraction, and can instead be based on a simplified planar structure. Eliminating the scaffold layer puts greater demand on the absorber. A mesoporous architecture generates the majority of carriers very close to the junction, but in a planar

*laurie.phillips@liverpool.ac.uk

structure it is possible for photo-excitation to take place deep in the material away from the electrical junction. Also, compared to mesoporous devices in which scattering is important, the absorption path length will be reduced in the planar configuration. However, in material of sufficient quality, the diffusion length for MAPI exceeds its absorption depth and therefore bulk recombination is expected to be low. Indeed, as the technology has progressed, device architecture has evolved from the dye-sensitized architecture (DSSC) to semiconductor-sensitized solar cells (SSSC), then to mesostructured solar cells (MSSC), and finally to planar structures. Planar morphology is particularly attractive, as it is easier to handle with rapid, low-cost fabrication techniques such as blade-coating and roll-to-roll processing.[11–13]

In planar thin-film photovoltaics, light is admitted through a transparent conducting oxide (TCO), then usually through an n-type window layer before being absorbed in a p-type absorber. Generally, the p-n junction formed by the window and absorber layer is highly asymmetric, due to the higher carrier density in the window layer, and only absorption in the p-type absorber contributes to the photocurrent. Therefore, it is possible to predict the maximum performance of a device by using a thin-film optical model to calculate the fraction of the incident photons absorbed after transmission through multiple partner layers, accounting for reflection and transmission losses and the effects of interference. The overall transmission through a layer stack is determined by the refractive index, n, extinction coefficient, k, and thickness of each layer. The approach taken here treats the device as a purely optical problem, thereby neglecting electrical effects. In particular, every photon absorbed in the MAPI layer is assumed to contribute an electron to the photocurrent. This gives an upper limit for the maximum J_{sc} available in an idealized cell, although comparing results with experimental devices is difficult due to the many sources of loss present in a real device.

Generally, MAPI films prepared by one- and two-step solution methods are too rough to allow high quality optical measurements. Therefore, in this work, MAPI thin films were deposited using an optimized technique to create ultra smooth layers suitable for variable angle spectroscopic ellipsometry (VASE). The wavelength-dependent complex refractive index, $N(\lambda) = n(\lambda) + ik(\lambda)$, was extracted from perovskite layers from fits to the VASE data and transmission spectrum. This in turn was deployed in a Python program, applying the transfer matrix method (TMM), to predict the maximum obtainable J_{sc} for planar structures. This was used to investigate the performance of structures incorporating TiO_2, WO_3, ZnO, Nb_2O_5, CdS, and $Cd_{0.6}Zn_{0.4}S$ window layers. By varying the thickness of each layer, performance maxima were identified for optimal device stacks in which the light absorbed in the MAPI layer was optimised. The peak positions provide design rules for choosing the layer thicknesses of planar devices in order to maximise J_{sc}.

2. Experimental

2.1. Fabrication of MAPI

A mixed solution containing 0.8 M PbI_2 and 0.4 M $PbCl_2$ in N,N-Dimethylformamide (DMF) was prepared and left stirring overnight at 70 °C to ensure it was completely dissolved. Substrates of 600 µm thick (100) silicon wafer from Siltronix™ were cleaned sequentially in an ultrasonic bath using distilled water with 5% Decon 90®, pure distilled water, and isopropyl alcohol (IPA) and dried in a nitrogen stream. The substrate then underwent a 5 minute oxygen plasma treatment to ensure a contaminant free surface with improved wetting properties for the subsequent deposition.[14]

The mixed lead-halide solution, kept at 70 °C, was deposited onto the room temperature substrate by spin-coating at 4000 rpm for 30 s in ambient conditions. A vapour-phase reaction process was used to convert the lead-halide layer into perovskite. The coated substrate was placed in the centre of a lidded petri-dish and surrounded by methylammonium iodide (MAI) powder. The dish was then placed inside a quartz tube, evacuated to a base pressure of $< 10^{-4}$ mTorr and heated to 120 °C for one hour. The converted black film was left to cool to room temperature in a nitrogen ambient, washed in IPA, and dried under a nitrogen stream. No post conversion annealing process was employed.

X-ray diffraction (XRD) analysis was performed on the films prepared using an identical methodology but on borosilicate glass substrates using a PANalytical™ X'Pert^3 Pro X-ray diffractometer at room temperature with Cu Kα radiation (λ = 0.15418 nm) in the 2θ range 10–75 ° with a step size of 0.01° and step time of 10 s. A JEOL™ JSM-7001F was used to perform electron microscopy on samples.

All chemicals were supplied by Sigma Aldrich™ with the exception of MAI, which was purchased from Solaronix SA®. All materials were used as received, without further purification processes.

2.2. Variable Angle Spectroscopic Ellipsometry

When light interacts with a layer of material, a change in polarization occurs. Spectroscopic ellipsometry measures the ratio of p- and s- polarized light from the reflected light (R_p and R_s respectively), recorded as the amplitude, Ψ, and phase difference, Δ, as in Equation 1.

$$\frac{R_p}{R_s} = \tan(\Psi)\exp^{i\Delta} \quad (1)$$

Variable angle spectroscopic ellipsometry (VASE) records the Ψ and Δ data for multiple angles of light incidence. A multi-oscillator model is used to fit the data from all the angles simultaneously. A good fit to the data, measured using a mean squared error (MSE), is required throughout the entire wavelength range. The sum of oscillators with the lowest MSE value is obtained through regression analysis with the aim of achieving a good fit (generally MSE <10) while using the minimum number of variables. The wavelength-dependent refractive index can be extracted from the model. Ellipsometry measurements were performed using a J. A. Woollam™ 2000M ellipsometer at 65°, 70°, and 75°. Φ and Δ were measured at room temperature in the wavelength range 241.1 nm to 1686.7 nm. Modelling of the data was performed using CompleteEASE™, software also from Woollam. The data was fitted with a Cauchy oscillator to find the thickness of the layer using the non-absorbing region of the spectra. Other parameters used starting values taken from literature,[15] but the fit was minimised without constraints.

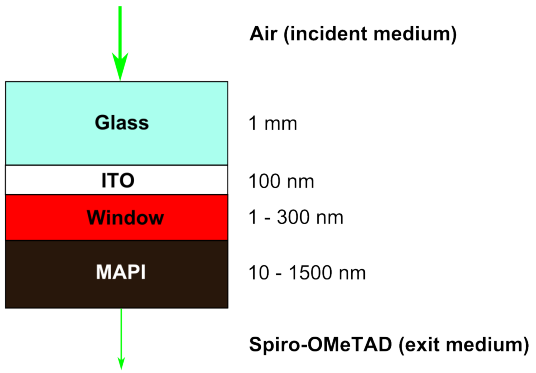

Figure 1: Schematic diagram of the solar cell structure modelled in this work. An optical model of the performance of this stack was used to investigate the choice of window layer material with TiO_2, WO_3, ZnO, Nb_2O_5, CdS, and $Cd_{0.6}Zn_{0.4}S$ being considered.

2.3. Optical Modelling

The aim of the modelling is to create a tool to to maximise J_{sc} via the optical design of the partner layers to the absorber, through which the light must pass. The model is capable of dealing with an arbitrary number and type of thin layers and can rapidly screen for optimum thicknesses and layer combinations. It is an optical only model which makes the following assumptions: a) the incident medium is assumed to be non-absorbing (i.e. the AM1.5 spectrum arrives at the cell unmodified), b) only light having $h\nu > E_g$ in the absorber is considered to contribute to J_{sc}, c) light is absorbed in the absorber with a quantum efficiency of 100% i.e. one photon produces one electron and there is assumed to be no recombination.

The 'Transfer Matrix Method' (TMM) was used for modelling the thin-film multilayer structures. It accounts for transmission, reflection and interference in the layers using a product of matrices and has been comprehensively described in a number of references including MacLeod.[16,17] The code, implemented in Python, computes the transmission of light from an incident medium (usually air or glass), through an arbitrary number of intermediate layers and into an exit medium. It takes the following as inputs: thickness range and dielectric constants for each layer, AM1.5 spectrum, and E_g of the absorber. The program then calculates the total transmission into the exit medium at each wavelength for every thickness in the computed range. This is then weighted using the AM1.5 spectrum and integrated up to the bandgap of the absorber to output a J_{sc} value for each thickness combination. We emphasise that the J_{sc} values calculated in this way represent the upper limits of performance expected from this optical-only model and do not take into account recombination and other electrical losses that are experienced in practical devices.

The structure being considered is shown in Fig. 1. It comprises a TCO-coated glass coversheet, being 100 nm of ITO on 1 mm of Optiwhite™ glass for all simulations. This is followed by an n-type window layer which is the object of the design optimisation in this work. The materials considered were TiO_2, WO_3, ZnO, Nb_2O_5, CdS, and $Cd_{0.6}Zn_{0.4}S$ with thicknesses in the range 1 - 300 nm. The ITO layer was found to attenuate the light with increasing thickness, but the interference fringes from adjusting this layer were an order of magnitude smaller than the window layer and therefore have been neglected in this study. For the absorber, MAPI thicknesses in the range 1 - 1500 nm were considered. An infinite layer of Spiro-OMeTAD was used as the exit medium.

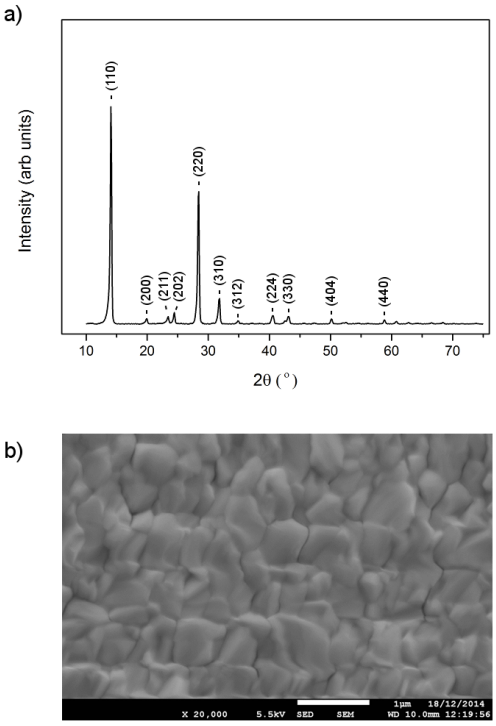

Figure 2: a) XRD data of a typical MAPI film showing many peaks with the (110), (220), and (310) peaks at 14.1°, 28.4°, and 32.1°, respectively, the most prominent b) SEM image taken of the MAPI layer surface showing the grain structure and coverage.

In order to use the transfer matrix method to calculate J_{sc} it was necessary to use a subtractive method. The output of the TMM is the light that reaches an infinite exit medium. Hence to calculate the light absorbed in a finite absorber we must calculate a) the total amount of light reaching the absorber from the partner layers and b) the remaining light after it has passed through the absorber layer thickness and beyond into an exit medium. The difference between these two values is the light absorbed by the MAPI layer which can then be converted to current and hence give a value for J_{sc}.

The optical model used in this work was implemented using Python 2.7. and will be made available, along with the n and k data for free use (see Appendix A).

3. Results & Discussion

3.1. MAPI Layer

The perovskite absorber films were characterised using XRD, SEM, and stylus profilometry to verify the crystal structure of the the material and measure the roughness of the layers. The typical XRD data in Fig. 2a

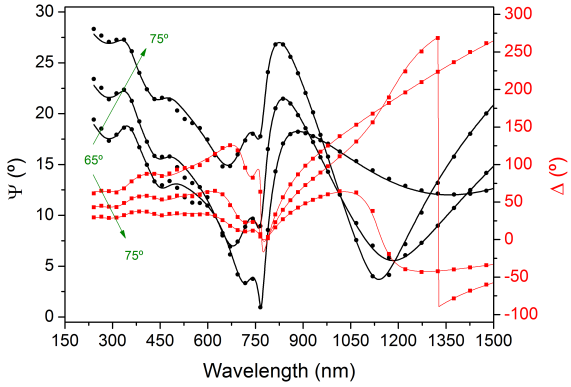

Figure 3: VASE data (dots) and fits (lines) to the Ψ (black, circles) and Δ (red, squares) measurements for a MAPI layer at three different angles of incidence; 65°, 70°, and 75°. MSE = 9.79.

most clearly shows reflections from the (110), (220), and (310) planes, giving peaks at 14.1°, 28.4°, and 32.1° characteristic of a highly ordered orthorhombic polycrystalline material. The SEM data in Fig. 2b show grains of ~500 nm in size forming a highly continuous layer.

Profilometry indicated an RMS roughness for these films of typically ~5 nm, with thickness 250±20 nm. This compares very favourably against films prepared by the two-step solution dip method which generally produces films with RMS roughness of 25 to 100 nm.[18,19] While there is great variability in the quality of films produced by the wide array of methods in the literature,[20] we conclude that MAPI films grown using the two-step vapour reaction method in this work have good crystallinity and superior smoothness and therefore are suitable for optical measurements.

3.2. Dispersion Relations

The optical properties of the MAPI layer were extracted by simultaneously fitting a multi-oscillator model to the Ψ and Δ ellipsometry measurements taken at three angles. The VASE data is shown in Fig. 3, along with fitting lines from the model (MSE = 9.79). The oscillator types and parameters used to fit the data are listed in Table 1.

To achieve a close-fit, the model required four oscillators: The first, modelled using a Tauc-Lorentz oscillator, represents the direct-bandgap transition from the highest valence band maximum to the conduction band minimum; The E_g value of ~1.55 eV from the fit is in good agreement with the literature.[21] The CPPB (critical-point parabolic-band) oscillators represent transitions arising from lower valence bands and have

Table 1: Table of parameters used to model the MAPI ellipsometry data, including the transition energy (ϵ_x), amplitude (A_x), and broadening (Γ_x) of each oscillator.

	Parameter	Value (eV)
Tauc-Lorentz	E_g	1.55
	ϵ_0	1.63
	A_0	23.9
	Γ_0	0.112
$CPPB_1$	ϵ_1	1.95
	$A1$	0.858
	Γ_1	1.37
$CPPB_2$	ϵ_2	3.44
	A_2	2.28
	Γ_2	1.31
Harmonic	ϵ_3	6.65
	A_3	4.75
	Γ_3	5.23

also been observed in other ellipsometry measurements on MAPI.[15,22–25] The harmonic oscillator represents a broad vibrational background. Dispersion relations were extracted from the model fits and are shown in Fig. 4.

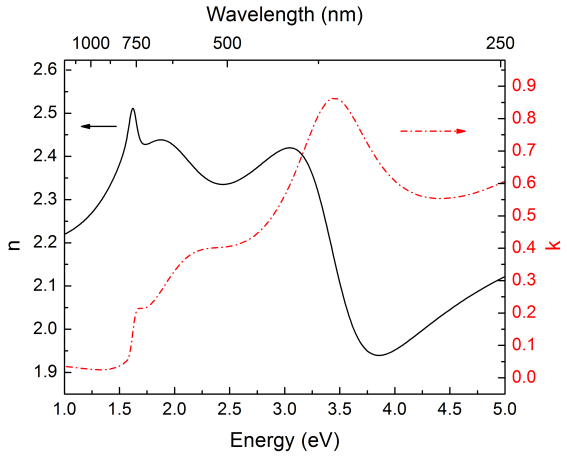

Figure 4: Dispersion relations for MAPI showing a sharp onset in the extinction coefficient at the bandgap, ~1.55 eV and further peaks from transitions at ~1.9 eV and ~3.4 eV.

The refractive index of MAPI has a peak around the bandgap at ~800 nm, and is lower compared to other semiconductor absorbers. For example, at 600 nm, the refractive indices are ~3.9 for Si and GaAs; ~3.0 for CdTe; and ~2.4 for MAPI. Indeed for MAPI, $n \approx 2.3$ for much of the visible range and so it will act as an excellent index-matching coating for silicon. This is one of the reasons why it is a promising candidate for the top cell in tandem devices. An additional benefit of the relatively low refractive index is that MAPI cells will have less need for an index matching layer themselves to minimise light lost to reflections at the front MAPI interface. The extinction coefficient, k, remains relatively high in the wavelength range 500 - 800 nm, matching or exceeding other common semiconductor absorber materials. For example at 600 nm, the extinction coefficients are: Si (0.03); GaAs (0.24); CdTe (0.31) and MAPI (0.37). This value for MAPI corresponds to a very high value of $\gtrsim 10^5$ cm^{-1} for the optical absorption coefficient for most of the range above the bandgap and hence the MAPI layer can be extremely thin while still absorbing most of the light.

3.3. *Optimizing the Window Layer*

Optical modelling has been used to investigate the optimum choice of window layer in order to maximise the J_{sc} obtained from a MAPI absorber layer in a planar solar cell. The structure modelled is shown in Fig. 1. Window layers comprising TiO_2, WO_3, ZnO, Nb_2O_5, CdS, and $Cd_{0.6}Zn_{0.4}S$ were investigated with their thicknesses being varied in the range 1-300 nm. In addition, the thickness of the MAPI absorber layer itself required for optimal operation was investigated in the range 1 - 1500 nm. Details of the calculation methods are given in Section 2.3.

The dependence of the J_{sc} on MAPI thickness is shown in Fig. 5 for an optimised thickness of TiO_2. It highlights the rapid onset of the J_{sc} as the MAPI thickness increases, as expected from the high absorption coefficient. Indeed, 85% of the light is absorbed at an absorber thickness of 350 nm while 90% is absorbed by 500 nm. In order to estimate the maximum J_{sc} obtainable for MAPI for this test structure, we therefore considered a MAPI thickness of 1 µm which is comparable to its minority carrier diffusion length. The value of J_{sc} = 23.81 mA cm^{-2} therefore represents an upper limit assuming zero recombination loss. Although in practice there will always be additional recombination loss, even in the highest quality material, this calculation is encouraging since the J_{sc} value is ~88% of that expected at the Schockley-Quiesser limit. With regard to the general form of the curve in Fig. 5 we note that: a) The strong absorption also mitigates interference effects in the absorber layer and hence only weak maxima and minima are visible in the curve, and b) Qualitatively similar results to those shown in Fig. 5 for the case

of TiO_2 were obtained for all the other window layer materials explored in this work.

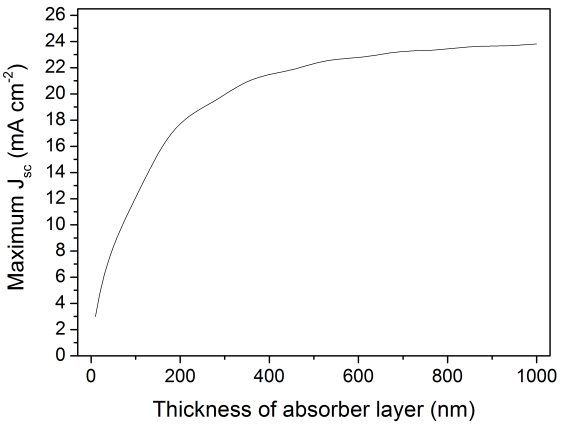

Figure 5: Modelling of the effect on J_{sc} obtained from MAPI as a function of thickness for a control structure (Fig. 1) having a 43 nm TiO_2 layer. 90% of the maximum output is achieved for a thickness of 500 nm.

The results of the J_{sc} modelling of window layer type (TiO_2, WO_3, ZnO, Nb_2O_5, CdS, and $Cd_{0.6}Zn_{0.4}$) and thickness are shown in the 3-D plots in Fig. 6, with the third axis being the MAPI thickness. It is clear from the graphs that all the wide bandgap oxides perform well optically and all show interference maxima due to changing the thickness of the window layer.

Table 2: Comparison of the maximum J_{sc} values and the optimized window layer thickness for each of the examined materials in the test structure outlined in Fig. 1.

	Max J_{sc} (mA cm^{-2})	Optimum thickness (nm)
TiO_2	22.31	43
WO_3	22.47	59
ZnO	22.04	60
Nb_2O_5	22.22	29
CdS	21.63	n/a
$Cd_{0.4}Zn_{0.6}S$	21.96	20

Cross-sections of the 3D plots were extracted for a MAPI thickness of 500 nm (i.e., the 90% absorption point) for each window layer, as shown in Fig. 7. Interference due to the window layer now has a significant effect and multiple peaks and troughs are visible in the J_{sc} as the thickness is varied. The difference between the peak and trough values depends on the Δn mismatch between window and MAPI. ΔJ_{sc} between the first peak and the following trough is slightly larger for ZnO (~0.94 mA cm^{-2}) than for the other oxides (TiO_2, WO_3, and Nb_2O_5) for which it is ~0.72 mA cm^{-2}. CdS has a different response as it absorbs at a much longer wavelength than the oxides with an E_g ~2.5 eV, and therefore the J_{sc} decreases rapidly with increasing thickness. However, by alloying CdS with ZnS, to create $Cd_{0.4}Zn_{0.6}S$, the bandgap increases to ~3.0 eV. This reduces the parasitic absorption and thus an interference pattern becomes observable that was not visible for CdS. Although $Cd_{0.4}Zn_{0.6}S$ has a fairly well matched refractive index to MAPI, there is still an increased level of absorption in it relative to the oxides, which restricts the J_{sc} values obtainable using this material.

A summary of the J_{sc} first maxima peak values from modelling is given in Table 2. From this, and Fig. 7, the following trends are apparent:

(a) All of the oxide materials have a first maximum of performance that exceeds the value of J_{sc} obtainable with no window.

(b) WO_3 is exceptional in that it maintains the J_{sc} advantage for all thicknesses in the range modelled, making it a good choice for a window layer.

(c) The other oxides (TiO_2, Nb_2O_5, and ZnO) all show a decrease in J_{sc} below the no-window value, in some regions. Hence for optimal use in devices, their thickness must be accurately controlled.

(d) CdS always acts to decrease the J_{sc} for all thicknesses and there are no interference maxima. CdS is therefore a poor choice of window from an optical standpoint.

(e) Use of the wider bandgap $Cd_{0.4}Zn_{0.6}S$ as an alternative to CdS recovers some of the losses but it remains inferior to the oxides.

All the materials examined in this study can be prepared using sputtering. While this is a vacuum process and therefore relatively expensive, it offers excellent control over thickness. However, if the window deposition could be incorporated into the glass manufacturing process i.e. in-line on a float glass manufacturing process, as is used for chemical vapour deposition (CVD) TCO coatings, then this would greatly reduce the cost. Alternatively, many of the materials are also able to be deposited via lower cost, solution-based methods including sol-gel, spin-coating,

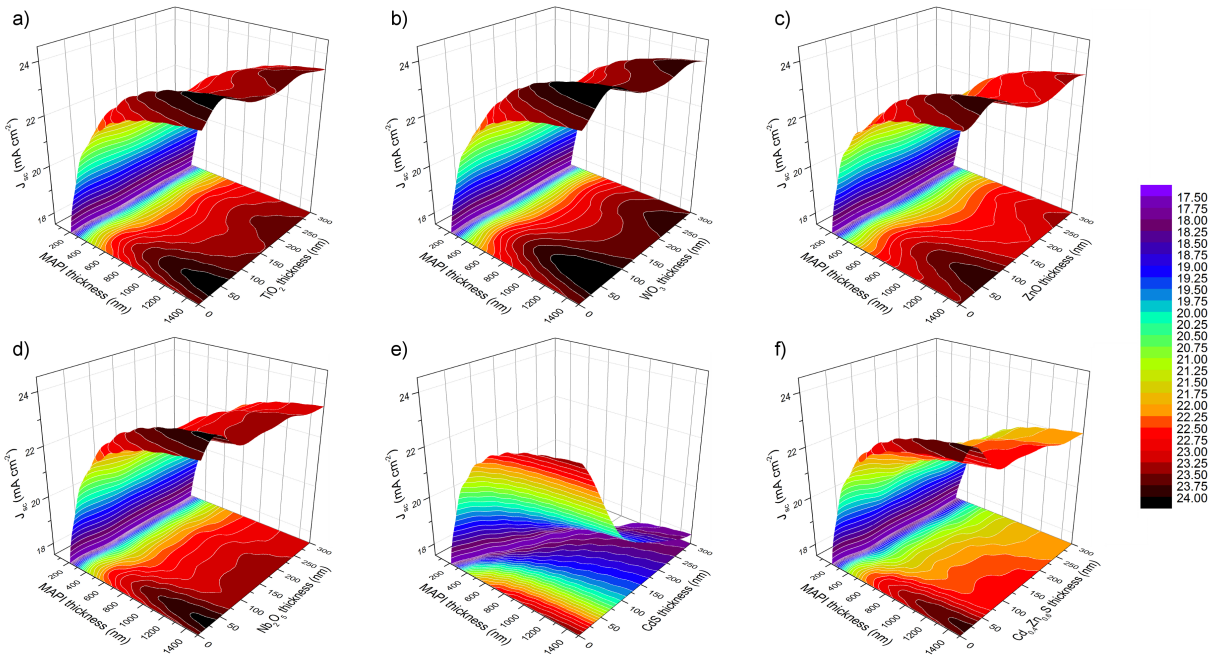

Figure 6: Three-dimensional plots of the upper limit of J_{sc} as a function of window and absorber layer thicknesses for a) TiO_2, b) WO_3, c) ZnO, d) Nb_2O_5, e) CdS), and f) $Cd_{0.6}Zn_{0.4}$

spray-coating and chemical bath deposition. While these methods have been used to create working devices with some of the materials,[18,26] they do not afford such high levels of thickness and uniformity control over a large area.

Finally it should be mentioned that while this optical study indicates some designs that could be used to maximise performance, electrical considerations are of course also paramount in the design of an efficient PV device. In particular, the band line ups (junction and contacts), conductivity of the material and the presence of interface states and deep levels are all influential on the position of the p-n junction and its efficiency in separating and collecting charge. It should also be borne in mind that it is possible in principle to engineer a true electrical heterojunction with collection from not only MAPI, as is considered here, but from its partner material as well. Nevertheless, the all optical model does provide some useful design rules to enhance the absorption in MAPI independent of the technological state of the control or optimisation of the electrical factors.

4. Conclusions

In summary, MAPI layers have been fabricated and a methodology identified to produce films with sufficient smoothness for accurate optical measurements. Variable angle spectroscopic ellipsometry was used to extract the refractive index and extinction coefficient from MAPI films. This data has been made publicly available in [ref data]. MAPI has a low refractive index compared to other solar cell absorbers (between ~2.3 and ~2.4 over the visible range) making it well suited as a potential top partner layer with silicon ($n \approx 3.9$) for use in tandem cells. A multi-layer optical-only model has been written, employing the transfer-matrix method, and used to calculate the transmission of light into the absorber layers of planar heterojunction solar cells having MAPI absorber layers. This code has been used to predict the maximal J_{sc} obtainable from planar solar cells using TiO_2, WO_3, ZnO, Nb_2O_5, CdS, and $Cd_{0.6}Zn_{0.4}S$ as window layers, and to identify the optimal thicknesses of each.

The best performing window material for the test structure under consideration was found to be WO_3, which achieved a maximum limiting J_{sc} of 22.47 mA cm^{-2} for a window layer thickness of 59 nm and a MAPI thickness of 500 nm. TiO_2, Nb_2O_5, and ZnO also demonstrated good optical performance, achieving a J_{sc} of 22.31, 22.04, and 22.22 mA cm^{-2} for window layer thicknesses of 43, 60, and 29 nm, respectively. CdS was shown to be a poor choice for window layer: Strong parasitic absorption meant that

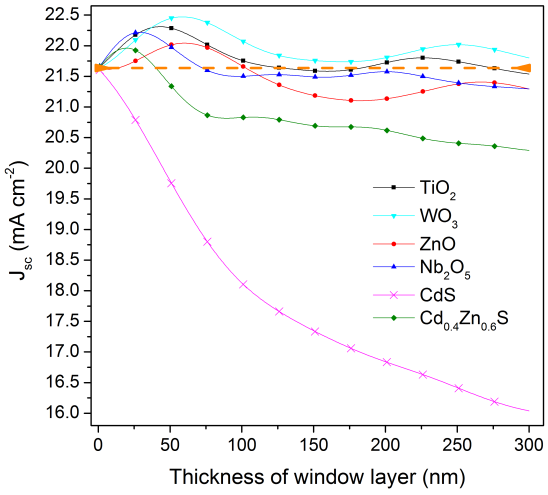

Figure 7: Comparison of the maximum J_{sc} available for variable window layer thicknesses with 500 nm MAPI absorber. The dashed orange line indicates the J_{sc} for the simulation without a window layer. This has been added as a guide to the eye to show the regions where the window layer enhances the possible current collection. A summary of the primary peaks and the corresponding window thicknesses extracted from these plots is given in Table 2.

the inclusion of CdS always acted to reduce the device performance and in contrast to the other materials, there was no peak observed for non-zero thicknesses of CdS. However, use of the higher gap alloy ($Cd_{0.4}Zn_{0.6}S$) allowed the optical performance to be improved over that of CdS, and a peak value of 21.96 mA cm^{-2} for a thickness of 20 nm could be achieved. Overall, the oxides tested here (TiO_2, WO_3, ZnO, Nb_2O_5) all performed better optically than the sulphides.

In all cases the most beneficial window layer performance from optical considerations alone was shown to be for thin layers of around $\lesssim$50 nm which corresponded to an interference first maximum value. Only WO_3 and TiO_2 demonstrated an optically beneficial effect from a window layer >100 nm in thickness, making these the most suitable choices for production as the other oxides require more critical control of the thickness. emphasising the importance of thickness and uniformity control for the oxide window layers. This study will serve to provide design information for future planar device structures, helping to maximise the J_{sc} of planar perovskite devices.

With the exception of WO_3, in order to exploit the interference effects observed in this study, the growth of continuous window layers with highly controlled thicknesses in the range 20 - 60 nm will be required. Presently it is popular to research the use of cheap solution-based methods for the deposition of both the absorber and window layers, for example spin-coating and spray pyrolysis. However, to enable the thickness control required here, it may be necessary use higher cost but more precise methods, such as sputtering and atomic layer epitaxy.

Acknowledgements

This research has been funded by EPSRC grants EP/J017361/1 and EP/M014797/1 (SUPERGEN). The authors thank Dr. Frank Jäckel for the use of a plasma cleaner.

Appendix A. Data

The n and k data for MAPI deposited on silicon extracted via VASE is available here [data in brief ref].

References

[1] M. M. Lee, J. Teuscher, T. Miyasaka, T. N. Murakami, H. J. Snaith, Efficient hybrid solar cells based on meso-superstructured organometal halide perovskites., Science (New York, N.Y.) 338 (2012) 643–7.

[2] H.-S. Kim, C.-R. Lee, J.-H. Im, K.-B. Lee, T. Moehl, A. Marchioro, S.-J. Moon, R. Humphry-Baker, J.-H. Yum, J. E. Moser, M. Grätzel, N.-G. Park, Lead iodide perovskite sensitized all-solid-state submicron thin film mesoscopic solar cell with efficiency exceeding 9%., Scientific reports 2 (2012) 591.

[3] J. M. Ball, M. M. Lee, A. Hey, H. J. Snaith, Low-temperature processed meso-superstructured to thin-film perovskite solar cells, Energy & Environmental Science (2013) 1739–1743.

[4] M. Liu, M. B. Johnston, H. J. Snaith, Efficient planar heterojunction perovskite solar cells by vapour deposition., Nature 501 (2013) 395–8.

[5] C. C. Stoumpos, C. D. Malliakas, M. G. Kanatzidis, Semiconducting tin and lead iodide perovskites with organic cations: Phase transitions, high mobilities, and near-infrared photoluminescent properties, Inorganic Chemistry 52 (2013) 9019–9038.

[6] S. D. Stranks, G. E. Eperon, G. Grancini, C. Menelaou, M. J. P. Alcocer, T. Leijtens, L. M. Herz, A. Petrozza, H. J. Snaith, Electron-hole diffusion lengths exceeding 1 micrometer in an organometal trihalide perovskite absorber., Science (New York, N.Y.) 342 (2013) 341–344.

[7] G. Xing, N. Mathews, S. Sun, S. S. Lim, Y. M. Lam, M. Grätzel, S. Mhaisalkar, T. C. Sum, Long-range balanced electron- and hole-transport lengths in organic-inorganic $CH_3NH_3PbI_3$., Science (New York, N.Y.) 342 (2013) 344–7.

[8] E. Edri, S. Kirmayer, A. Henning, S. Mukhopadhyay, K. Gartsman, Y. Rosenwaks, G. Hodes, D. Cahen, Why Lead Methylammonium Tri-Iodide Perovskite-Based Solar Cells Require a Mesoporous Electron Transporting Scaffold (but Not Necessarily a Hole Conductor), Nano Letters 14 (2014) 1000–1004.

[9] J. Shi, J. Dong, S. Lv, Y. Xu, L. Zhu, J. Xiao, X. Xu, H. Wu, D. Li, Y. Luo, Q. Meng, Hole-conductor-free perovskite organic lead iodide heterojunction thin-film solar cells: High efficiency and junction property, Applied Physics Letters 104 (2014) 063901.

[10] V. D'Innocenzo, G. Grancini, M. J. P. Alcocer, A. R. S. Kandada, S. D. Stranks, M. M. Lee, G. Lanzani, H. J. Snaith, A. Petrozza, Excitons versus free charges in organo-lead tri-halide perovskites., Nature communications 5 (2014) 3586.

[11] G. Hodes, D. Cahen, Photovoltaics: Perovskite cells roll forward, Nature Photonics 8 (2014) 87–88.

[12] J. H. Kim, S. T. Williams, N. Cho, C.-c. Chueh, A. K.-Y. Jen, Enhanced Environmental Stability of Planar Heterojunction Perovskite Solar Cells Based on Blade-Coating, Advanced Energy Materials 5 (2015).

[13] K. Hwang, Y.-s. Jung, Y.-j. Heo, F. H. Scholes, S. E. Watkins, J. Subbiah, D. J. Jones, D.-y. Kim, D. Vak, Toward Large Scale Roll-to-Roll Production of Fully Printed Perovskite Solar Cells (2015).

[14] L. Jiang, S. Li, J. Wang, L. Yang, Q. Sun, Z. Li, Surface wettability of oxygen plasma treated porous silicon, Journal of Nanomaterials 2014 (2014).

[15] J. M. Ball, S. D. Stranks, M. Hoerantner, S. Hüttner, W. Zhang, E. Crossland, I. Ramirez, M. Riede, M. B. Johnston, R. Friend, H. Snaith, Optical Properties and Limiting Photocurrent of Thin-Film Perovskite Solar Cells, Energy Environ. Sci. (2014) 1–3.

[16] H. A. Macleod, Thin-Film Optical Filters, Third Edition, Series in Optics and Optoelectronics, Taylor & Francis, 2001.

[17] S. Guldin, Inorganic Nanoarchitectures by Organic Self-Assembly 19 (2013) 19–33.

[18] D. Liu, M. K. Gangishetty, T. L. Kelly, Effect of $CH_3NH_3PbI_3$ Thickness on Device Efficiency in Planar Heterojunction Perovskite Solar Cells, J. Mater. Chem. A (2014).

[19] K. Liang, D. Mitzi, M. Prikas, Synthesis and characterization of organic-inorganic perovskite thin films prepared using a versatile two-step dipping technique, Chemistry of Materials 4756 (1998) 403–411.

[20] J. Berry, T. Buonassisi, D. a. Egger, G. Hodes, L. Kronik, Y.-L. Loo, I. Lubomirsky, S. R. Marder, Y. Mastai, J. S. Miller, D. B. Mitzi, Y. Paz, A. M. Rappe, I. Riess, B. Rybtchinski, O. Stafsudd, V. Stevanovic, M. F. Toney, D. Zitoun, A. Kahn, D. Ginley, D. Cahen, Hybrid Organic-Inorganic Perovskites (HOIPs): Opportunities and Challenges, Advanced Materials (2015).

[21] T. Baikie, Y. Fang, J. M. Kadro, M. Schreyer, F. Wei, S. G. Mhaisalkar, M. Graetzel, T. J. White, Synthesis and crystal chemistry of the hybrid perovskite $(CH_3NH_3)PbI_3$ for solid-state sensitised solar cell applications, Journal of Materials Chemistry A 1 (2013) 5628.

[22] Q. Lin, A. Armin, R. C. R. Nagiri, P. L. Burn, P. Meredith, Electro-optics of perovskite solar cells, Nature Photonics (2014).

[23] Q. Chen, H. Zhou, Z. Hong, S. Luo, H.-S. Duan, H.-H. Wang, Y. Liu, G. Li, Y. Yang, Planar Heterojunction Perovskite Solar Cells via Vapor-Assisted Solution Process, Journal of the American Chemical Society 136 (2014) 622–625.

[24] X. Ziang, L. Shifeng, Q. Laixiang, P. Shuping, W. Wei, Y. Yu, Y. Li, C. Zhijian, W. Shufeng, D. Honglin, Y. Minghui, G. G. Qin, Refractive index and extinction coefficient of $CH_3NH_3PbI_3$ studied by spectroscopic ellipsometry, Optical Materials Express 5 (2014) 29.

[25] P. Löper, B. Niesen, J. Werner, S.-J. Moon, M. Filipič, M. Topič, Y. Yum, S. D. Wolf, C. Ballif, Complex refractive index of methyl ammonium lead halide determined from spectroscopic ellipsometry, J. Phys. Chem. Lett. (2015).

[26] E. J. Juarez-Perez, M. Wuβler, F. Fabregat-Santiago, K. Lakus-Wollny, E. Mankel, T. Mayer, W. Jaegermann, I. Mora-Sero, Role of the Selective Contacts in the Performance of Lead Halide Perovskite Solar Cells, The Journal of Physical Chemistry Letters 5 (2014) 680–685.